Cronfa - Swansea University Open Access Repository

_____

This is an author produced version of a paper published in:
Journal of The Royal Society Interface

_____

_____

Cell Geometry across the Ring Structure of Sitka Spruce

T. P. S. Reynolds[1], H. C. Burridge[2], R. Johnston[3], G. Wu[4], D. U. Shah[5], O. A. Scherman[4], P. F. Linden[6], and M. H. Ramage[5]

[1]Institute for Infrastructure and Environment, School of Engineering, University of Edinburgh, Edinburgh EH9 3FG, UK

[2]Department of Civil and Environmental Engineering, Imperial College London, London SW7 2AZ, UK

[3]Materials Research Centre, College of Engineering, Swansea University, Swansea SA1 8EN

[4]Melville Laboratory for Polymer Synthesis, Department of Chemistry, University of Cambridge, Lensfield Road, Cambridge CB2 1EW, UK

[5]Department of Architecture, University of Cambridge, Cambridge CB2 1PX, UK

[6]Department of Applied Mathematics and Theoretical Physics, University of Cambridge, Centre for Mathematical Sciences, Wilberforce Road, Cambridge CB3 0WA, UK

April 20, 2018

Abstract

For wood to be used to its full potential as an engineering material, it is necessary to quantify links between its cell geometry and the properties it exhibits at bulk scale. Doing so will make it possible to predict timber properties crucial to engineering, such as mechanical strength and stiffness, and the resistance to fluid flow, and to inform strategies to improve those properties as required, as well as to measure the effects of interventions such as genetic manipulation and chemical modification. Strength, stiffness and permeability of timber all derive from the geometry of its cells, and yet current practice is to predict them based on properties, such as bulk density, that do not directly describe the cell structure. This work explores links between micro-computed tomography data for structural-size pieces of wood, which show the variation of porosity across the wood's ring structure, and high-resolution tomography showing the geometry of the cells, from which we measure cell length, lumen area, porosity, cell wall thickness and the number density of cells. High-resolution scans, while informative, are time-consuming and expensive to run on a large number of samples at the scale of building components. By scanning the same volume of timber at both low and high resolutions (high-resolution scans over a near-continuous volume of timber of approximately 20mm^3 at 15μm^3 per voxel), we are able to demonstrate correlations between the measurements at the two different resolutions, reveal the physical basis for these correlations, and demonstrate that the data from the low-resolution scan can be used to estimate the variation in (small-scale) cell geometry throughout a structural-size piece of wood.

1   Background and Summary

The internal structure of a softwood like Sitka spruce makes it effective both as a conduit for fluid transport and as a structural material: multifunctional tracheid cells with high aspect ratio make up over 90% of the volume of the wood, and provide a flow path through their lumina, and structural support through a thickened secondary cell wall. Groups of ray cells allow fluid flow in the radial direction and resin ducts form in spaces between cells. All these cells contribute to the structural and flow performance of the wood. The scale of both the lumina and the cell walls varies depending on the stage of the growing season at which a particular portion of the wood was laid down. Wood laid down early in the growing season, so called 'earlywood', contains larger lumina and thinner cell walls than that of 'latewood' and as such is expected to exhibit different structural and fluid transport properties [Siau, 1984].

The empty lumina in dry wood make it a lightweight and efficient structural material, with a strength-to-weight ratio along the axis of the trunk comparable to that of steel [Ramage et al., 2017]. In the use of wood for engineering, the flow paths, as well as the structural resistance, are important: wood can be impregnated with fluid treatments for preservation, or to enhance its performance. Few treatment processes achieve any substantial degree of impregnation, however, with most wood treatment occurring at or near surface. Accurate modelling of flow is required to design treatment processes, which in turn requires a thorough understanding of cell geometry.

Measurement of cell geometry can also improve understanding of the load-resistance of wood [Bjurhager, 2008, Gibson, 2012]. Gibson [2012] describes how plants achieve a wide range of mechanical properties by alterations to this geometry as well as changes to the composition of the cell wall. Qing and Mishnaevsky [2010] present a series of numerical models extending from the arrangement of cellulose in the cell wall through the shape of tracheid cells to the ring structure in a softwood. Malek and Gibson [2017] present numerical models which also incorporate the effect of other cell types to bring out the nonlinear relationship between density and elastic modulus in balsa wood. Such research enables the development of relationships between cell geometry and bulk structural properties of timber [Mishnaevsky and Qing, 2008, Hofstetter and Gamstedt, 2009, de Borst et al., 2012, De Borst and Bader, 2014, Malek and Gibson, 2017]. This well-developed field of research shows the promise that, if the geometry of cells can be accurately measured, then, in conjunction with information about the molecular architecture of the cell wall, the strength and stiffness of wood can be predicted. Microtomography of timber at the structural scale cannot currently measure cell geometry directly, but using a suitable relationship between larger-scale microtomography and cell geometry, a prediction of bulk structural properties could be possible. The present study proposes such a relationship, and demonstrates how it can be applied to Sitka spruce softwood.

A multi-scale understanding of the geometry of wood can enable the development of new wood products which make the best use of the natural structure of the material, and could also improve the process of timber grading. Grading structural timber requires properties that can be measured quickly and without damage, the *indicating properties*, which correlate well with the strength and stiffness properties of the timber [Ridley-Ellis et al., 2016], some of which can

not be measured without damaging the material. The present process of grading structural timber uses properties such as bulk density and bending stiffness as indicating parameters, but cell geometry would seem a promising candidate, since it represents a more fundamental property of the wood, and in-situ loading with microtomography has enabled observation of behaviour of the cells responsible for structural failure of wood [Zauner et al., 2012, Baensch et al., 2015]. A commercial system now exists for X-ray CT scanning of logs prior to sawmilling [Ridley-Ellis et al., 2016], which suggests that its large-scale implementation in grading could be economically feasible.

In order to realize the potential for accurate prediction of the properties of structural timber based on measurements correlated with cell geometry, it is necessary to make a link between measurements made at the bulk scale on structural-size pieces of timber, and those that can distinguish and measure individual cells. This study uses X-ray micro-computed tomography (μCT) to construct an image of the internal structure of Sitka spruce, *Picea sitchensis*, at those two scales.

Previous studies using CT scanning of plant material can be divided into those concerned with the cell structure of the material, and those concerned with larger features. Studies of larger features investigate knots and splits in sawn timber [Schad et al., 1996], adhesive joints in glued-laminated timber [Sterley et al., 2013], and fluid content [Fromm et al., 2001] or transport of fluid through wood [Žlahtič et al., 2017]. These studies use spatial resolutions in the range of 100 to 400μm and, therefore, only show the variation in density across the growth rings in a softwood, but do not distinguish cell walls.

Microtomography of the cellular structure, on the other hand, has been used to measure the penetration of adhesive or other fluids [Sterley et al., 2013, Sedighi Moghaddam et al., 2017], the mechanisms in the cells which control the movement of fluid [Derome et al., 2009, Bouche et al., 2016] and the response of the individual cells to applied load [Zauner et al., 2016]. Since hardwood has vessels, which have a relatively large cross-sectional area, they were the first to be distinguished as X-ray microtomography developed. Steppe et al. [2004] measure vessel geometry in hardwoods by an image segmentation technique, with results verified by inspection and direct measurement from the images. Image segmentation was later applied to the more densely-packed tracheid cells in softwood [Mayo et al., 2010] and the fibre, ray and vessel cells in hardwood [Sedighi Moghaddam et al., 2017]. Sedighi Moghaddam et al. [2017] distinguish cell types by their geometry, and determine the distribution of cell wall thickness and porosity for each cell type in each specimen and Mayo et al. [2010] measure porosity and orientation of cells in earlywood and latewood. They do not measure the length of the cells, which requires scans with both sufficient resolution to distinguish the cell walls, and sufficient length along the longitudinal axis of the cells to see their full extent. This is a challenge for cells which can have an aspect ratio of 100 or more.

Cell length and diameter in softwood and hardwood has been widely reported before. One way of generating these data is the time-consuming process of manually measuring cells from physically and chemically macerated wood under a light microscope [Fujiwara and Yang, 2000]. Alternatively, optical fibre analysers are used, which allow a rapid and automated analysis of samples, and this technique has been used to build up a picture of fibre geometry across different species [Li et al., 2011, Mvolo et al., 2015] and throughout a complete

tree [Yemele et al., 2015]. These studies show that cell length varies from the centre of the tree, increasing through the juvenile wood and becoming relatively constant in mature wood. Fibre analysers operate on wood pulp, thus losing the structure and arrangement of the material before measurement [Li et al., 2011]. μCT scanning offers the opportunity to rapidly measure the geometry of hundreds of cells throughout a volume of intact wood.

In this study, three-dimensional scans are used to enable characterisation of cell morphometry throughout a series of volumes covering a complete growth ring, and several complete cell lengths. These scans were carried out specifically to estimate the porosity of the wood, the distributions of lumen cross-sectional area, and the length of the cells in a set of specimens for which fluid impregnation tests were conducted by Burridge et al. [forthcoming].

Darcy's law describes fluid flow in porous media by their permeability, the driving pressure and the viscosity of the fluid. It has been shown to be inaccurate to represent flow in wood by this single permeability parameter [Bramhall, 1971, Banks, 1981]. The field is rather less developed than the structural analysis of wood, and the progress through multi-scale modelling is less advanced. Zillig et al. [2006], Mendoza et al. [2012] develop meso-scale models representing earlywood and latewood, cross grain transport and grain angle. The thesis of Zillig [2009] moves towards multi-scale modelling, concluding that "in modelling of liquid transport, the cellular level needs to be taken into account".

The model by Petty [1970] is based on the physical microstructure of the wood. The set of models by Burridge et al. [forthcoming] extend that of Petty [1970] by incorporating capillary action and a statistical representation of the parameters of the cell geometry of the wood, including lumen area and cell length, and their variation through the ring structure. The methods in the present study provide those geometrical parameters, and their statistical distributions at locations across the ring structure of the wood.

Although our specimens were small (10mm by 10mm by 70mm in the longitudinal direction of the cells) compared to wood sections used in structural applications, they contained more than one growth ring, and thus captured a large variation in cell geometry. As with structural-size timber, a scan with sufficient resolution to show the cellular structure across the whole specimen was not feasible either in terms of scan time or data storage capacity. For example, the sub-specimen used for cell length measurement had a file size of 12GB when reconstructed with 8-bit resolution, and had a scan time of approximately 20 hours, and its volume was three orders of magnitude smaller than the complete specimen. We, therefore, first carried out scans with a low resolution, covering the entirety of each specimen, and then cut up those specimens to allow additional high-resolution scans to provide data for the geometry of the cells. We then examined the relationship between data gathered from low-resolution scans and the measured cell geometry from our high-resolution scans, correlating the two to allow an estimation of the variation of cellular geometry across the whole specimen. As a result, this analysis provides measurements of tracheid geometry throughout the ring structure of a softwood.

2 Materials and Methods

The wood used in this study was kiln-dried Sitka spruce (*Picea sitchensis*) supplied by BSW Timber Ltd (Newbridge, Wales). Its moisture content was measured by the oven-dry method to be approximately 12%. Three specimens, 10mm by 10mm by 70mm in the longitudinal direction, were CT-scanned at low resolution over their entire volumes. The three-dimensional image of the specimen is made up of cubic voxels (three-dimensional pixels), which for this scan had a side length of 52.73μm. The output of the scan is the X-ray attenuation coefficient for each voxel, which is proportional to the mean density of material in that volume. Each specimen was weighed and its dimensions measured before scanning, so that its weight and dimensions could be used to calibrate the correlation between their measured X-ray attenuation coefficient and CT number. The measured bulk density of each specimen was compared to the mean attenuation coefficient of its image, and there was sufficient variation in density between the three specimens to validate this calibration. The high-resolution scan required a smaller sub-specimen, for which a 15mm length section along the grain was removed from each specimen. A grid was scored onto the surface to enable accurate location of the sub-specimens to be cut from these 15mm lengths. The sub-specimens were approximately 1.5mm by 1.5mm by 15mm along the grain. The sub-specimens were then cut using a razor blade through the score lines. An image was taken of the scored grid, which was transferred onto the low-resolution scan, as shown in Figure 1**a**. High-resolution scans were then carried out on these sub-specimens, with a voxel of sides approximately 2μm. Slices from five of the high-resolution scans are shown in Figure 1**b**. This process ensured that the position of each high-resolution scan was known within the volume of the corresponding low-resolution scan. For the high-resolution scans, the three-dimensional cell geometry could be identified (such as in Figure 1 panel **c**) with every voxel assigned either to be part of the solid cell wall or void space.

2.1 Low-resolution scans of the ring structure

For the low-resolution scan, all three specimens were imaged together to ensure the most accurate comparison of the linear attenuation coefficient measured by CT for each specimen. The method is described in S2. The linear attenuation coefficient could then be converted to a CT number using the measured weight of each specimen and its dimensions. Since the voxel size for these scans was too large to identify the cell walls individually, the CT number was used to indicate the proportion of solid material and void space in each voxel, or alternatively the porosity. The true porosity in each region was then found using the high-resolution scans on sub-specimens and correlated with the CT number at low resolution. The specimens were identified, separated and images of individual specimens were rotated so that the ring structure was aligned with the pixel coordinates for ease of processing and analysis. Figure 2**a** defines the axes used to describe the orientation of specimens and images in this paper. The radial, tangential and longitudinal planes are defined as the planes to which the axes are normal. Across the 10mm by 10mm face of the specimen, the curvature of the rings was not significant, and the variation in CT number due to the rings could therefore be considered to occur along the radial direction. As shown in
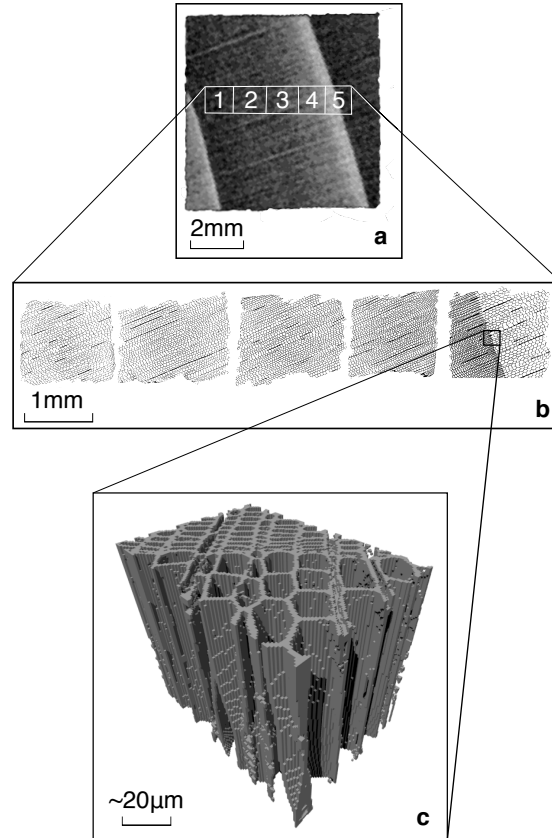
Figure 1: Relating specimens and scans across scales, to correlate whole-specimen scans with the measured cellular geometry. **a** is a slice from the low-resolution scan of Specimen 2 (light-greys mark the highest densities), **b** shows a line of the high-resolution scans on the sub-specimens taken from that specimen (since the solid cell walls are black, the highest density appears darker here) and **c** shows a three-dimensional rendering of all the voxels identified as being part of the cell wall in a small volume of material
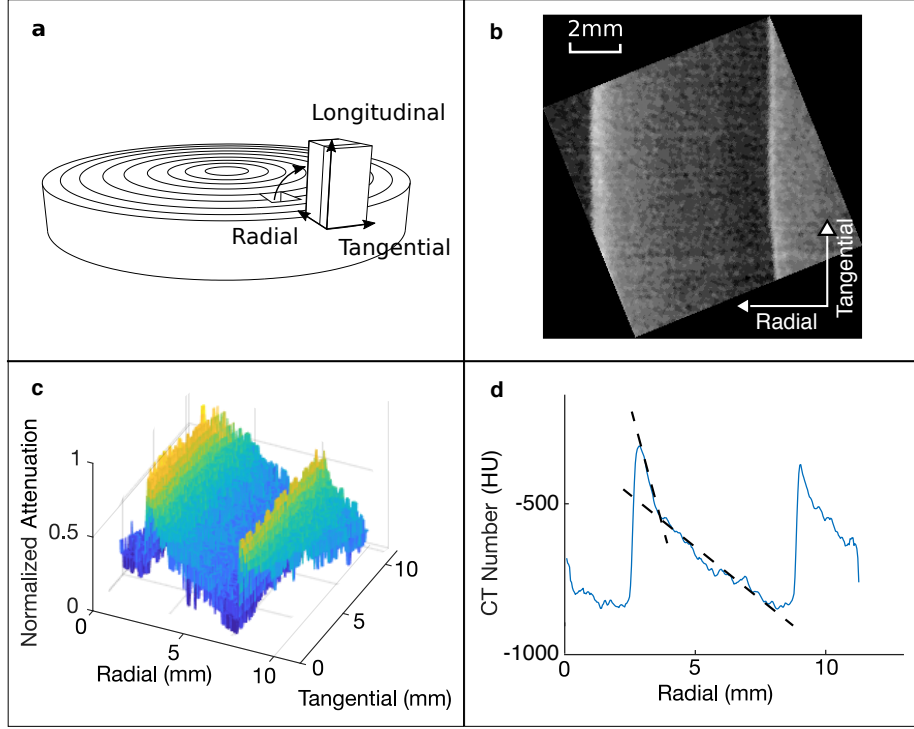
Figure 2: **a** shows the orientation of the radial, tangential and longitudinal directions in a slice of the trunk. CT scan data at low resolution in **b** and **c** show the variation in CT number across ring structure - dotted lines in **d** show the gradients of linear fits to particular regions. The wood was laid down from right to left by the tree.

Figure 2 panels **b** and **c**, with the rings aligned vertically, there is no apparent systematic variation of CT number in the tangential direction, so the noise can be dealt with most simply by averaging along this direction, giving a mean variation of density across the ring structure as shown in Figure 2**d**.

The variation in CT number across the cross-section is shown in Figure 2**d**. The cells at the right hand edge of the image were grown first. Moving from right to left, the (volumetric) growth rate slows as the tree lays down latewood cells and the CT number increases to a peak (thin vertical white band). The growth then stopped over winter, before restarting in spring at a rapid growth rate as the tree laid down new earlywood cells, with a higher porosity, resulting in a lower CT number (vertical dark band in Figure 2**b**). The CT number then increases gradually towards the next peak, and so on. There is, therefore, a clear boundary between latewood and earlywood in each ring as illustrated by the sharp changes from high to low values of CT number shown in Figure 2**d**, which we refer to as the 'winter transition'.

Conversely, as the wood cells are laid down during a given growing season the change from earlywood to latewood is gradual. Havimo et al. [2008] use the radial diameter of trachieds to measure this gradual transition between earlywood and latewood in Norway Spruce. They note that there is a change in

7

gradient between the two phases, with a much lower gradient in the earlywood phase. Figure 2**d** shows that a change in the gradient of CT number with radial position is apparent at approximately -525 HU in these specimens, but the data also shows that there is still a marked gradient throughout the earlywood. From all of our low-resolution scan data, the mid-point between the extremes of CT number is at approximately -525 HU. Throughout, we define the threshold between earlywood and latewood to occur at a CT number of -525 HU.

2.2 High-resolution scans of the cellular geometry

The μCT method is described in S2. A total of seven sub-specimens were scanned. An image segmentation process was used on the three-dimensional μCT images, to identify each of the tracheid cells, and to assign each voxel either to a cell lumen, or to the cell wall. The segmentation is based on a three-dimensional watershed transform of the image stack produced by μCT (also applied to plant cells by Willis et al. [2016]). The segmented image was then used to measure the dimensions of each cell lumen. The analysis comprised a 6.4mm-long scan crossing the winter transition between earlywood and latewood, which showed a number of complete cells sufficient for the statistical distribution of their length to be ascertained and compared between earlywood and latewood. In addition, a series of six 2mm-long scans at varied radial locations and from different specimens enabled the variation of the small-scale geometry across the ring structure to be determined.

2.3 Morphometry analysis

The steps of the image processing are shown in Figure 3. These two-dimensional images show the tangential plane, as defined in Figure 2**a**, and illustrate the three-dimensional segmentation process. The detailed process of producing a binary image of solid cell wall material and void space, applying a Euclidian distance transform and then carrying out watershed segmentation is described in S1.

For each high-resolution scan, the distribution of each measured parameter could then be assessed. The mean cross-sectional area of the cell was estimated by dividing its volume (measured as the number of voxels assigned to that cell) by its length (the distance between the furthest spaced voxels). The aspect ratio is estimated as $L/\sqrt{A}$, where A is the cross-sectional area of the lumen and L is the length. A representative cross-sectional area for each cell lumen was calculated by dividing the volume of the lumen by its length. This gave an advantage over two-dimensional methods which take a set of measurements at a plane, and thus measure some cell lumina at their tapered ends. Some 'cells' identified by segmentation were radial cells or artefacts of the analysis, and so the aspect ratio was used to separate out the slender, longitudinal tracheid cells which provide the main structural function and flow paths in the material. Cells with an aspect ratio less than 10 were removed before analysis.

The width of the cell wall can be estimated from the porosity and the number density of cells in the cross-section, by assuming a cell shape. Two possible assumed cell shapes, a regular hexagon and a square, are shown in Figure 4. These represent two extremes of geometry used for micromechanical modelling of cells [Mishnaevsky and Qing, 2008]. The combined area of the lumen and the
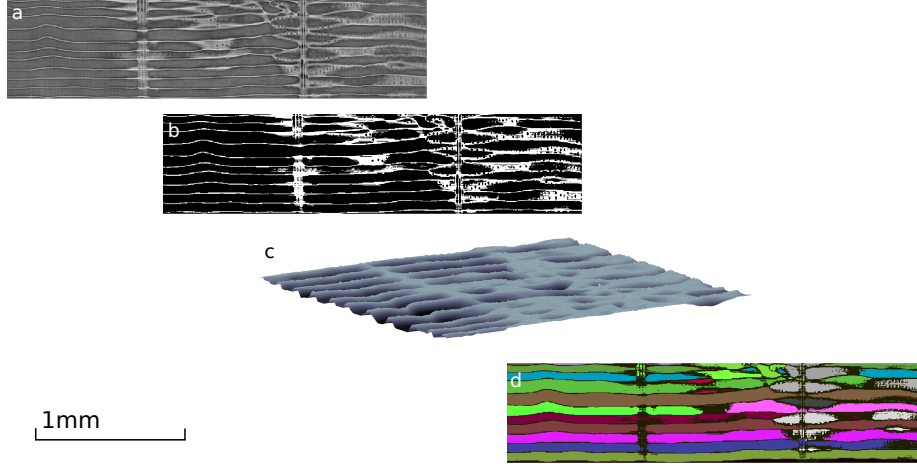
Figure 3: The main steps of the segmentation process: **a** shows the raw greyscale image data from the CT scan; **b** is the binarised image in which cell wall material is distinguished from pore space; **c** is the Euclidian distance transform of the binary image, used for segmentation; and **d** is the segmented image, with cell lumina assigned a random colour

cell wall A_c is given by the inverse of the number density of cells in cells per mm^2. The area of the cell wall A_w is then given by $A_w = (1 - p)A$, where p is the porosity. The geometry of the cell for either assumed shape provides an equation for the cell wall thickness w,

$$w_h = \sqrt{\frac{2A}{\sqrt{3}}} \left(1 - \sqrt{p}\right) \quad \text{and} \quad w_s = \sqrt{A} \left(1 - \sqrt{p}\right), \tag{1}$$

where the subscripts h and and s correspond to the hexagonal or square shape, respectively. The wall thicknesses calculated for the two geometries differ by less than 8%.

3 Results and Discussion

Figure 5**a** shows the a cross-section of the μCT image either side of the winter transition, and the corresponding segmented image for each is shown in Figure 5**b**, with each cell assigned a random colour. Figure 5**c** shows the segmentation result from the scan covering the longest length along the cell axis. The upper image of Figure 5**c**, shows the tangential plane, in which each cell is aligned with the ones either side of it, since they are produced from the same parent cell in the cambium of the tree as it increases in diameter. In the lower image, a section at 90° to the one above it showing the radial plane, the cells overlap and are randomly arranged. This is characteristic of Sitka spruce, since the parent cells are arranged with overlap. Species with this feature are described as having a *nonstoried* cambium. This illustrates one of the benefits of this method over analysis based on two-dimensional images. As noted by Sarén et al. [2001], for a nonstoried cambium, the random arrangement of cells in the radial plane
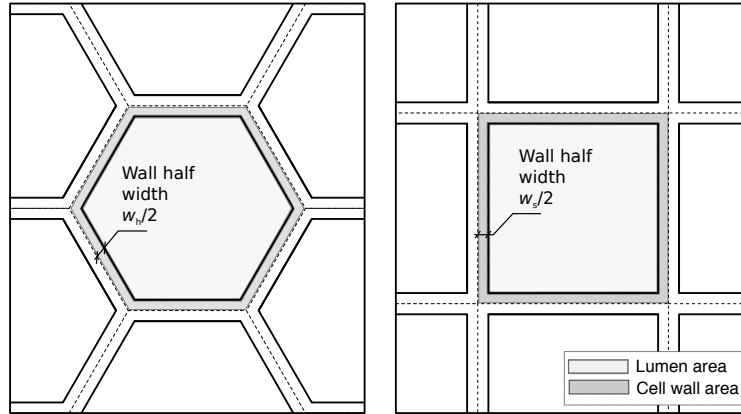
Figure 4: Simplified cell geometry assuming either a regular hexagonal cell or a square, showing the lumen and cell wall area assigned to a particular cell.

means that any two-dimensional section of the wood in the longitudinal plane will generally include cells cut through near their narrow tip, and this will give an underestimate of the cross-sectional area of that cell. By considering the entire volume of each cell, we measure a representative cross-sectional area over its whole length, and thus avoid this problem.

Once the cells were identified in the high-resolution scans, and their position in the low-resolution scan was known, it was possible to examine the relationship between position in the ring structure and cell morphometry. Figure 6 shows the histograms of lumen cross-sectional area for five neighbouring regions of wood, together spanning an entire growth ring, from the first earlywood at **1** to the latewood (up to the winter transition) at **5**. The histograms show a systematic decrease in the mean area from **1** to **5**. This is consistent with the low-resolution data in Figure 2**d** which showed no plateau of CT number in the ring structure to suggest a homogeneous region of either earlywood or latewood. However, panels **1** to **3** in Figure 6 show that the variation in mean area of cell lumen across the earlywood part of the ring is small compared with the variability in each histogram. Expressing these three volumes as a single phase of wood could be reasonable in certain applications. In panels **4** and **5**, a contrast is evident moving into the latewood region, with a substantial reduction in the mean area of lumina, and in the variance of area.

The distributions of cell dimensions were then linked to the value of the CT number measured at the same point in the specimen in the low-resolution scans. Having measured the total volume associated with lumina within our high-resolution scans we could calculate the porosity of any given region. Figure 7**b** shows the variation of measured porosity with CT number. Each datum represents the mean of one complete high-resolution scan. Assuming that the material density of solid cell wall does not vary (for example with porosity), a linear relationship between CT number and porosity is expected. The data show reasonable agreement with a linear relationship (Figure 7**b**) and so we regard this assumption to be valid. The least-squares fitted linear relationship in Figure 7**b** has a CT number of 712 HU for a porosity of zero, equivalent to a bulk density of 1712kg/m^3. The oven dry density of the solid cell wall in softwood is
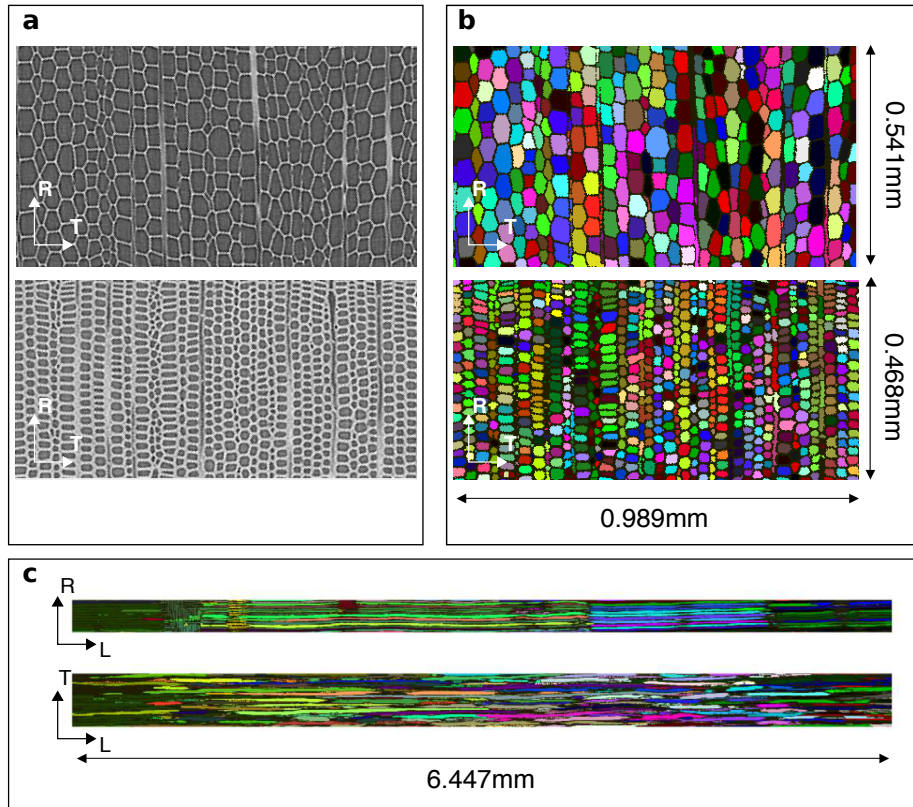
Figure 5: Segmented images: **a** the original CT scan data for the earlywood (top) and latewood (bottom) side of the winter transition; **b** the corresponding segmented images, with cells identified with a random colour; and **c** a longitudinal view showing the full length of the cells in latewood for a tangential (top) and radial (bottom) section. R indicates the radial direction, T the tangential and L the longitudinal.
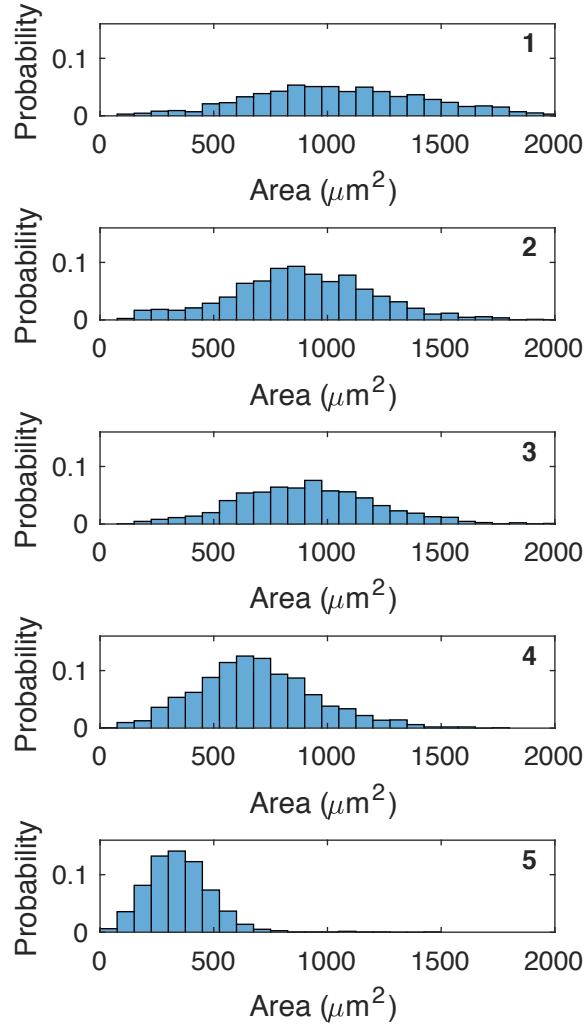
Figure 6: Histograms of lumen cross-sectional area from high-resolution scan on sub-specimens **1** to **5** from specimen 2, shown in Figure 1 **a** - only the latewood part of **5**, before the winter transition, is included.

approximately 1500kg/m^3 [Moore, 2011], and increases with moisture content [Zauer et al., 2013]. The moisture content of these specimens, at 12%, would not result in a 12% increase in cell wall density, because of swelling of the cell wall, but the intercept for zero porosity is likely to be within 10% of the expected value.

The greyscale images were converted to binary cell wall – void space using a threshold filter based on the average intensity in the region. This means that in regions with high cell wall content, and therefore high intensity, the binary threshold is raised slightly, leading to a tendency to increase the measured porosity. This would tend to change the gradient of the fitted relationship, and result in a higher value of the intercept for zero porosity. The observation that the fitted curve has an intercept for zero porosity close to the expected cell wall density gives some confidence that any artificial increase in porosity in areas of high cell wall content is not severe.

The total void space in a given cross-section may also be calculated by multiplying the mean (cross-sectional) area of cell lumina (for example in mm^2) by the number density of cells (for example in mm^{-2}). This procedure, carried out over a representative sample of cross-sections, provides a method for estimating the porosity. Thus, if the relationships between both the area of cell lumina and CT number, and the number density of these cells and CT number, can be approximated by power laws, then the exponents of the two power laws must sum to unity; i.e. the product of the two relationships must be linear (Figure 7b).

The number density of cells within the specimens is approximately 500 mm^{-2} in the most porous wood and increases to approximately 1000 mm^{-2} in the least porous and so the exponent in the power law relating these must be greater than zero. Our data for the mean area of the cell lumena and the number density of cells (Figures 7a and 7c, respectively) are not sufficient to determine the precise exponent of the power laws. Arbitrarily setting the exponent in both power laws to 0.5 provides a reasonable fit to both data sets — see the green curves in Figures 7a and 7c — reassuringly, this highlights that our analysis yields results which are not inconsistent with physical constraints. Furthermore, we note that the product of these two power-laws yields a linear fit between the porosity and CT number which is approximately 10% lower than the results plotted in Figure 7b; this difference is to be expected, since we deliberately included only tracheid cells in our analysis of the high-resolution scan data and thereby excluded the pore space associated with, for example, ray cells. Within Figure 7a we plot the best fits for power laws with exponents of 0.5 and 1.0 (i.e. linear). The difference between these two fits (with distinctly different exponents) over the range of values of interest is always less than 5%. For simplicity, we therefore adopt a linear fit to map CT number in the low-resolution scans to a prediction of lumina area.

In contrast to the relationship between CT number and porosity, there is not a unique physical relationship between cell lumina area and CT number: the same CT number could result from either a low number density of large lumina with thick cell walls or a high number density of smaller lumina with thin cell walls. The fact that lumina cross-sectional area and CT number are well correlated (Figure 7a) suggests that other fixed patterns in the cellular structure exist, e.g. the cell wall thickness and number density of cells also vary with the porosity (and hence CT number). We hypothesize that the relationships are,
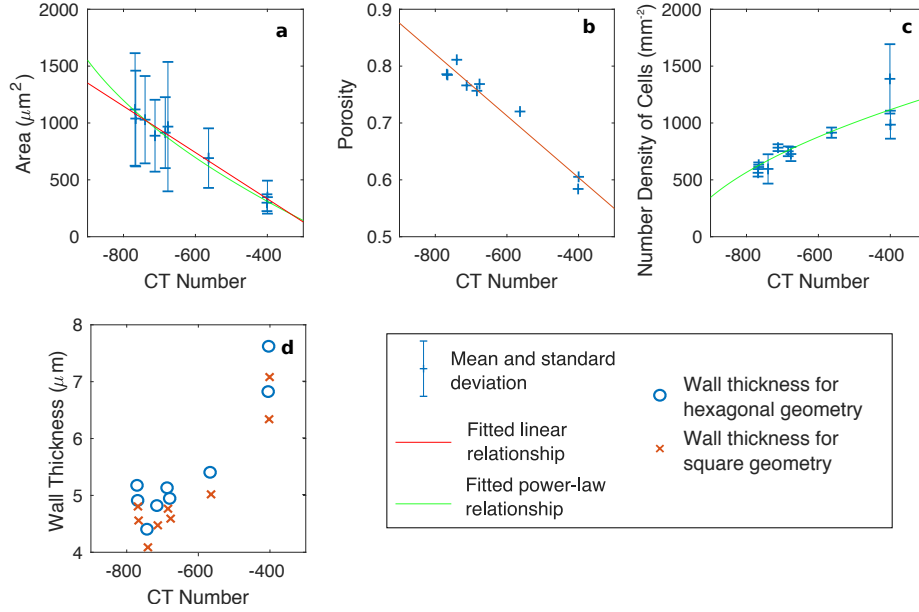
Figure 7: Measured cell geometry: **a** to **d** show the relationship between CT number in the low-resolutions scans (measured at the relevant location) and the measured cell properties from the high-resolution scans of each of the sub-specimens. Two specimens were split either side of the winter transition, giving nine points.

in fact, unique within a species or within a species grown in a certain location, and the data we have collected so far support that hypothesis, since the area of cell lumina is proportional to CT number, even within different specimens. A full characterisation of the pattern of geometry in the wood requires accurate measurements of those parameters.

The estimates of cell wall thickness calculated using the two methods detailed in Equation (1) are plotted in Figure 7**d**, the difference due to the choice of method is of the same order as the variations between sub-specimens of similar porosity/CT number. The data for wall thickness showed too much scatter to justify fitting and mapping onto the low-resolution scans, but they are plotted in Figure 7**d** to show that such a mapping would be possible given more reliable data on the number density of cells. We assert that a segmentation process which also identifies radial cells could enable this.

The approximate linear relationships determined from the data of the high-resolution scans (Figures 7**a** and 7**b**) were used to map the data from the low-resolution scans onto estimates of both the porosity and lumen areas. In so doing we were able to provide estimates of the small-scale properties, i.e. lumen areas, for the complete specimens — the data from which is presented in Table 1.

Figure 8 shows that the tracheid length does not vary across the winter transition between earlywood and latewood: the mean length is 2.46mm for earlywood, with a coefficient of variation of 0.24, and 2.50mm for latewood, with
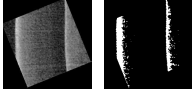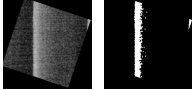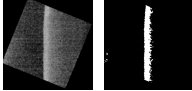
14

		Proportion	Porosity	Lumen Area μm^2
Specimen 1	Entire specimen	—	0.73 (0.09)	787 (0.30)
	Earlywood	$\alpha = 0.83$	0.75 (0.06)	867 (0.20)
	Latewood	$1 - \alpha = 0.17$	0.63 (0.05)	415 (0.27)
Specimen 2	Entire specimen	—	0.75 (0.08)	869 (0.26)
	Earlywood	$\alpha = 0.88$	0.76 (0.05)	930 (0.17)
	Latewood	$1 - \alpha = 0.12$	0.63 (0.04)	417 (0.21)
Specimen 3	Entire specimen	—	0.75 (0.07)	873 (0.24)
	Earlywood	$\alpha = 0.89$	0.76 (0.05)	923 (0.16)
	Latewood	$1 - \alpha = 0.11$	0.63 (0.03)	436 (0.17)

Table 1: Parameters from measured cell geometry mapped onto complete specimens, as mean values with coefficient of variation in brackets where applicable. Areas identified as latewood are shown in white in the right hand image of each specimen.
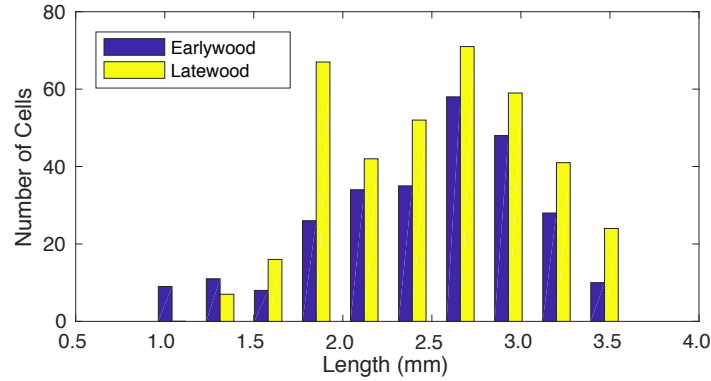
Figure 8: Comparison of length measurements of tracheids in adjacent early-wood and latewood volumes
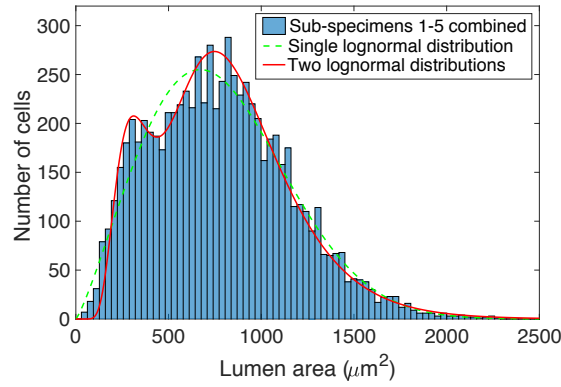

Figure 9: Histogram combining the (7,610) lumen areas plotted within figure 6 which span one entire growth ring. The best-fit log-normal distribution is marked by the green dashed curve. The distribution obtained by classifying the data into earlywood and latewood phases, fitting each phase to a log-normal distribution, and summing these fits produces the distribution marked by the red solid curve.

a coefficient of variation of 0.22. These parameters are taken to be representative for these specimens, and fit within the range for mature wood of 2.1mm to 3.1mm reported by Brazier [1967] for UK-grown Sitka spruce.

The variation in CT number across the specimen does not show a boundary between two separate homogeneous phases of less porous 'latewood' and 'earlywood' in these specimens, but a change in gradient is apparent which can be used to distinguish between the two. For some applications, it may not be necessary to distinguish between phases of wood, since a CT scan can give a CT number at every point throughout its volume, which may be mapped onto a variation in other properties, such as lumen area and porosity.

For many applications, the distinction between phases is important [Burridge et al., forthcoming]. Application to flow modelling, for example, requires a distinction between earlywood and latewood, since information taken from literature on the number, geometry and probability of aspiration of bordered

pits is specific to earlywood and latewood phases [Phillips, 1933, Liese and Bauch, 1967, Ahmed et al., 2013]. Moreover, for both flow modelling and micro-mechanical models, even in the absence of the need to consider two distinct phases, it may be necessary to accurately represent the statistical distribution of the micro-structure geometry (e.g. cell wall thickness, lumen area), which often proves challenging.

The histogram of the measurements of lumen area across the ring structure from Figure 6 (specimen 2, sub-specimens 1–5) is plotted in Figure 9. Since the areas must follow a single-sided distribution (i.e. take strictly positive values) one might expect to represent the data using, for example, a lognormal distribution (which is relatively common in nature and can be expected under either the central-limit theorem or maximum entropy arguments [Lyon, 2013]). However, the fit of the data to a single lognormal distribution is poor. On the other hand, fitting separate lognormal distributions, X, to the lumen areas to each of the earlywood, X_e, and latewood, X_l, data provides a simple means of achieving a good fit to the data. Figure 9 shows the fit achieved taking the volume weighted average of the two lognormal distributions according to: $n[\alpha X_e + (1 - \alpha)X_l]$, where n is the number of cells sampled; values for the means and variances of the lognormal distributions, and the value of α (the proportion of earlywood), are all taken from the data of specimen 2, sub-specimens 1–5.

For each specimen, every voxel can be assigned a porosity and a distribution of lumen cross-sectional area, mapped according to the relationships shown in Figure 7. The resulting parameters for earlywood and latewood in each specimen are shown in Table 1. As expected these measurements, taken across an entire specimen, do not show such a stark distinction between earlywood and latewood as would be expected for the material immediately to each side of the winter transition, as shown in Figure 5. This is because these parameters are the mean for each phase when all of the ring structure is classified as either earlywood or latewood and there is substantial variation in each phase.

The extremes of porosity across the ring structure are better seen in Figure 7. At approximately 0.58 and 0.81, they correspond to CT numbers of -740 HU and -401 HU, and bulk densities of 260kg/m^3 and 599kg/m^3, which fit well within the range of values measured for UK-grown Sitka spruce by Brazier [1967].

4   Conclusions

We have measured the variation in CT number across the ring structure of soft-wood specimens using low-resolution scans, and determined the size and shape of softwood tracheids at high resolution, by X-ray micro-computed tomography and image processing. The subsequent data was used to show the extent to which the CT number measured across the ring structure for low-resolution imaging can be correlated to the geometry of the cellular structure that makes up the wood. Using the correlation between CT number and both porosity and cell cross-sectional area, shown in Figure 7, it has been possible to map the measured CT number throughout specimens with complete growth rings onto corresponding values of cross-sectional area and porosity. The correlation between CT number and cell cross-sectional area is not determined by any physical constraint: it appears to be a pattern of growth in the wood. Further research

17

is required to identify the bounds within which this correlation holds: it may be true for all trees of a particular species, or all those grown in a particular climate.

It is intended that this mapping from the cell structure to measurements which could be made at the scale of structural timber, provides a step towards linking the bulk engineering properties of timber to its fundamental underlying structure. Ultimately this would lead to better multi-scale modelling of wood, more rigorous grading of structural timber and more effective design of processes which involve fluid flow through wood, such as impregnation and drying.

We have discussed the merit of describing this wood in terms of earlywood and latewood phases. There is a gradual transition of CT number across an annual ring, and this is reflected in a gradual transition of cell lumen area across the five sub-specimens studied across the ring structure, as shown in Figure 6. However, the distribution of lumen areas across the ring as a whole is shown in Figure 9 to be well represented by the sum of two lognormal distributions, and this insight may be useful in wood modelling in various fields.

Our finding that there is no significant variation in cell length within the ring structure, shown in Figure 8, is reasonable given that the cells are laid down sequentially by the same initial cells, and this has been shown in previous studies. The present study shows that μCT can provide this data for volumes of intact wood incorporating several hundred cells. This information is crucial in the modelling of fluid transport in wood, since good estimates of the cell lengths and their statistical distribution in different parts of the wood enable a more accurate estimate for the number of bordered pits between cells (which provide the greatest restriction to fluid flow) that fluid must pass through along a given flow path.

5 Acknowledgments

6 Data, code and materials

Supplementary material describing the segmentation process are included as S1. The greyscale images which form the CT scan data are available at DOI: 10.7488/ds/2260, along with Matlab code for segmentation.

7 Competing interests

The authors have no competing interests.

References

S. A. Ahmed, L. Hansson, and T. Morén. Distribution of preservatives in thermally modified scots pine and norway spruce sapwood. Wood Science and Technology, 47(3):499–513, 2013. ISSN 00437719. doi: 10.1007/s00226-012-0509-4.

F. Baensch, M. Zauner, S. J. Sanabria, M. G. R. Sause, B. R. Pinzer, A. J. Brunner, M. Stampanoni, and P. Niemz. Damage evolution in wood: Synchrotron radiation micro-computed tomography (SRμCT) as a complementary tool for interpreting acoustic emission (AE) behavior. Holzforschung, 69(8):1015–1025, 2015. ISSN 1437434X. doi: 10.1515/hf-2014-0152.

W. B. Banks. Addressing the problem of non-steady state liquid flow in wood. Wood Sci. Technol., 15(3):171–177, 1981.

I. Bjurhager. Mechanical behaviour of hardwoods - effects from cellular and cell wall structures. PhD thesis, Royal Institute of Technology (KTH), Sweden, 2008.

P. S. Bouche, S. Delzon, B. Choat, E. Badel, T. J. Brodribb, R. Burlett, H. Cochard, K. Charra-Vaskou, B. Lavigne, S. Li, S. Mayr, H. Morris, J. M. Torres-Ruiz, V. Zufferey, and S. Jansen. Are needles of Pinus pinaster more vulnerable to xylem embolism than branches? New insights from X-ray computed tomography. Plant Cell and Environment, 39(4):860–870, 2016. ISSN 13653040. doi: 10.1111/pce.12680.

G. Bramhall. The validity of Darcy's law in the axial penetration of wood. Wood Sci. Technol., 5(2):121–134, 1971.

J. D. Brazier. Timber Improvement II: The Effect of Vigour on Young-Growth Sitka Spruce. Forestry, 40(2):117–128, 1967. ISSN 0015-752X. doi: 10.1093/forestry/40.2.117.

H. Burridge, G. Wu, T. P. S. Reynolds, D. Shah, R. Johnston, O. A. Scherman, M. H. Ramage, and P. F. Linden. The liquid transport in softwood: timber as a model porous medium and natural material. Nature Communications, forthcoming.

K. De Borst and T. K. Bader. Structure-function relationships in hardwood - Insight from micromechanical modelling. Journal of Theoretical Biology, 345:78–91, 2014. doi: 10.1016/j.jtbi.2013.12.013.

K. de Borst, T. K. Bader, and C. Wikete. Microstructure-stiffness relationships of ten European and tropical hardwood species. Journal of Structural Biology, 177(2):532–542, 2012. doi: 10.1016/j.jsb.2011.10.010.

D. Derome, W. Zillig, and J. Carmeliet. Multi-scale modeling for moisture transport in wood. In Sixth Plant Biomechanics Conference, Cayenne, 2009.

J. H. Fromm, I. Sautter, D. Matthies, J. Kremer, P. Schumacher, and C. Ganter. Xylem water content and wood density in spruce and oak trees detected by high-resolution computed tomography. Plant physiology, 127(October):416–425, 2001. ISSN 0032-0889. doi: 10.1104/pp.010194.

S. Fujiwara and K. C. Yang. The Relationship between Cell Length and Ring Width and Circumferential Growth Rate in Five Canadian Species. IAWA Journal, 21(3):335–345, 2000. doi: 10.1163/22941932-90000251.

L. J. Gibson. The hierarchical structure and mechanics of plant materials. Journal of The Royal Society Interface, 9(76):2749–2766, nov 2012. ISSN 1742-5689. doi: 10.1098/rsif.2012.0341.

M. Havimo, J. Rikala, J. Sirviö, and M. Sipi. Distributions of tracheid cross-sectional dimensions in different parts of Norway spruce stems. Silva Fennica, 42(1):89–99, 2008.

K. Hofstetter and E. K. Gamstedt. Hierarchical modelling of microstructural effects on mechanical properties of wood. A review. COST Action E35 2004-2008: Wood machining - Micromechanics and fracture. Holzforschung, 63(2):130–138, 2009. doi: 10.1515/HF.2009.018.

B. Li, R. Bandekar, Q. Zha, A. Alsaggaf, and Y. Ni. Fiber quality analysis: OpTest fiber quality analyzer versus L&W fiber tester. Industrial and Engineering Chemistry Research, 50(22):12572–12578, 2011. doi: 10.1021/ie201631q.

W. Liese and J. Bauch. On the closure of bordered pits in conifers. Wood Science and Technology, 1(1):1–13, 1967. ISSN 00437719. doi: 10.1007/BF00592252.

A. Lyon. Why are normal distributions normal? Br. J. Philos. Sci., 65(3):621–649, 2013.

S. Malek and L. J. Gibson. Multi-scale modelling of elastic properties of balsa. International Journal of Solids and Structures, 113-114:118–131, 2017. ISSN 00207683. doi: 10.1016/j.ijsolstr.2017.01.037.

S. C. Mayo, F. Chen, and R. Evans. Micron-scale 3D imaging of wood and plant microstructure using high-resolution X-ray phase-contrast microtomography. Journal of Structural Biology, 171(2):182–188, 2010. doi: 10.1016/j.jsb.2010.04.001.

M. Mendoza, P. Hass, F. K. Wittel, P. Niemz, and H. J. Herrmann. Adhesive penetration of hardwood: a generic penetration model. Wood Sci. Technol., 46(1-3):529–549, 2012.

L. Mishnaevsky and H. Qing. Micromechanical modelling of mechanical behaviour and strength of wood: State-of-the-art review. Computational Materials Science, 44(2):363–370, 2008. doi: 10.1016/j.commatsci.2008.03.043.

J. Moore. Wood properties and uses of Sitka spruce in Britain. Technical report, Edinburgh, jan 2011.

C. S. Mvolo, A. Koubaa, J. Beaulieu, A. Cloutier, and M. J. Mazerolle. Variation in wood quality in white spruce (Picea glauca (Moench) Voss). Part I. defining the juvenile-mature wood transition based on tracheid length. Forests, 6(1):183–202, 2015. doi: 10.3390/f6010183.

J. Petty. Permeability and structure of the wood of sitka spruce. Proc. R. Soc. Lond. B, 175(1039):149–166, 1970.

E. W. J. Phillips. Movement of the pit membrane in coniferous woods, with special reference to preservative treatment. Forestry, 7:109–120, 1933.

H. Qing and L. Mishnaevsky. 3D multiscale micromechanical model of wood: From annual rings to microfibrils. International Journal of Solids and Structures, 47(9):1253–1267, 2010. doi: 10.1016/j.ijsolstr.2010.01.014.

M. H. Ramage, H. Burridge, M. Busse-Wicher, G. Fereday, T. Reynolds, D. U. Shah, G. Wu, L. Yu, P. Fleming, D. Densley-Tingley, J. Allwood, P. Dupree, P. Linden, and O. Scherman. The wood from the trees: The use of timber in construction. Renewable and Sustainable Energy Reviews, 68(October 2015): 333–359, 2017. doi: 10.1016/j.rser.2016.09.107.

D. Ridley-Ellis, P. Stapel, and V. Baño. Strength grading of sawn timber in Europe: an explanation for engineers and researchers. European Journal of Wood and Wood Products, 74(3):291–306, 2016. ISSN 1436736X. doi: 10.1007/s00107-016-1034-1.

M. P. Sarén, R. Serimaa, S. Andersson, T. Paakkari, P. Saranpää, and E. Pesonen. Structural variation of tracheids in norway spruce (Picea abies [L.] Karst.). Journal of Structural Biology, 136(2):101–109, 2001. doi: 10.1006/jsbi.2001.4434.

K. C. Schad, D. L. Schmoldt, and R. J. Ross. Nondestructive Methods for Detecting Defects in Softwood Logs. Technical report, Forest Products Laboratory, Madison, WI, 1996.

M. Sedighi Moghaddam, J. Van den Bulcke, M. E. Wålinder, P. M. Claesson, J. Van Acker, and A. Swerin. Microstructure of chemically modified wood using X-ray computed tomography in relation to wetting properties. Holzforschung, 71(2), 2017. ISSN 1437-434X. doi: 10.1515/hf-2015-0227.

J. F. Siau. Transport processes in wood. Springer-Verlag, 1984.

K. Steppe, V. Cnudde, C. Girard, R. Lemeur, J. P. Cnudde, and P. Jacobs. Use of X-ray computed microtomography for non-invasive determination of wood anatomical characteristics. Journal of Structural Biology, 148(1):11–21, 2004. ISSN 10478477. doi: 10.1016/j.jsb.2004.05.001.

M. Sterley, E. Serrano, B. Enquist, and J. Hornatowska. Finger Jointing of Freshly Sawn Norway Spruce Side Boards – A Comparative Study of Fracture Properties of Joints Glued with Phenol-Resorcinol and One-Component Polyurethane Adhesive. In S. Aicher, H. W. Reinhardt, and H. Garrecht, editors, RILEM Bookseries 9 - Materials and Joints in Timber Structures, pages 325–339. RILEM, 2013.

L. Willis, Y. Refahi, R. Wightman, B. Landrein, J. Teles, K. C. Huang, E. M. Meyerowitz, and H. Jönsson. Cell size and growth regulation in the Arabidopsis thaliana apical stem cell niche. Proceedings of the National Academy of Sciences, 113(51):E8238–E8246, dec 2016. ISSN 0027-8424. doi: 10.1073/pnas.1616768113.

M. C. Yemele, J. Beaulieu, M. Defo, A. Koubaa, A. Cloutier, and C. S. Mvolo. Prediction of tracheid length and diameter in white spruce (Picea glauca). IAWA Journal, 36(2):186–207, 2015. doi: 10.1163/22941932-00000095.

M. Zauer, A. Pfriem, and A. Wagenführ. Toward improved understanding of the cell-wall density and porosity of wood determined by gas pycnometry. Wood Science and Technology, 47(6):1197–1211, 2013. ISSN 00437719. doi: 10.1007/s00226-013-0568-1.

M. Zauner, D. Keunecke, R. Mokso, M. Stampanoni, and P. Niemz. Synchrotron-based tomographic microscopy (SbTM) of wood: Development of a testing device and observation of plastic deformation of uniaxially compressed Norway spruce samples. Holzforschung, 66(8):973–979, 2012. ISSN 00183830. doi: 10.1515/hf-2011-0192.

M. Zauner, M. Stampanoni, and P. Niemz. Failure and failure mechanisms of wood during longitudinal compression monitored by synchrotron microcomputed tomography. Holzforschung, 70(2):179–185, 2016. doi: 10.1515/hf-2014-0225.

W. Zillig. Moisture transport in wood using a multiscale approach. PhD thesis, Katholieke Universiteit Leuven, 2009.

W. Zillig, H. Janssen, J. Carmeliet, and D. Derome. Liquid water transport in wood: towards a mesoscopic approach. In Research in Building Physics and Building Engineering, pages 107–114. London: Taylor & Francis, 2006.

M. Žlahtič, U. Mikac, I. Serša, M. Merela, and M. Humar. Distribution and penetration of tung oil in wood studied by magnetic resonance microscopy. Industrial Crops and Products, 96:149–157, 2017. ISSN 09266690. doi: 10.1016/j.indcrop.2016.11.049.

S1 Segmentation process

The segmentation process was carried out on high-resolution scans, with a voxel size ranging from 1.04 to 2.49μm. The scans covered a volume approximately 1mm $\times$ 1mm $\times$ 2mm, with the exception of a multi-scan batch reconstruction approximately 6.4mm long allowing analysis of cell length.

Two of the scans were carried out at the interface of earlywood and latewood, and these were split into earlywood and latewood sections. This was necessary because a different depth limit was used for earlywood and latewood in the H-minima transform during segmentation.

The three-dimensional image was then converted to a binary image using Matlab's *imbinarize()* function with the adaptive setting, which compares the greyscale level (proportional to CT number) of each voxel to the mean greyscale level in a neighbourhood around that voxel. If the level in that voxel is more than half the mean, then it is marked as binary one, else it is binary zero. The only user-selected parameter in this process is therefore the size of the region chosen to include several complete cells, for which we used a side length of 101 voxels. The calculated porosity is relatively insensitive to this choice: taking, for example, specimen 2 sub-specimen 1 we determine the porosity to be 0.745, alternatively using a region of side length of 51 voxels gives a porosity of 0.753 and taking a side length of 151 voxels gives a porosity of 0.744.

The binary image then contained predominantly cell walls marked as binary one, with binary zero in the void space. Small groups of pixels in the void space were incorrectly identified as being part of the cell wall. Since all the cell walls form a single continuous group of voxels, the noise may be reduced by setting to zero all voxels not part of a large group. Connectivity was defined using a 6-connected neighbourhood: that is, two voxels are considered to be connected if one is in one of the six locations immediately adjacent to the other in three dimensions. This was done using Matlab's *bwareaopen()* function.

A Euclidian distance transform was then applied, creating a greyscale image where the grey level indicates the distance to the nearest voxel with binary one. The watershed segmentation was used on this image, identifying catchments for each local minimum greyscale level in the image, but before doing so, three processes were carried out on the image to mitigate against oversegmentation:

- An asymmetrical averaging filter was applied to allow for the high aspect ratio of the cells, and surpress multiple minima along their length: a filter with aspect ratio 10:1:1 is applied with the long direction along the length of the cells.

- Minima which were not sufficiently distinct from the voxels around them were surpressed using an H-minima transform through Matlab's *imhmin()* function.

- The cell walls were superimposed on the image with a value of infinity, to ensure they did not form part of any region.

The watershed transform could then be carried out using Matlab's *watershed()* function. Figure 5 shows each cell marked with a random colour to illustrate the segmentation. The segmented image was inspected for over- or under- segmentation, and the parameter for *imhmin()* was altered accordingly.

If the image was oversegmented, then the parameter was increased to surpress more local minima, and vice versa. Values of 1.5 for latewood and 3 for earlywood were generally found to give accurate segmentation, with the lower value for latewood reflecting the smaller cell cross-sections, and therefore the smaller Euclidian distance values.

S2   Micro-computed Tomography

The low-resolution scans were carried out using a lab-based Nikon XT H225 microfocus X-ray microtomography system, with a 1.3 Megapixel Varian PaxScan 2520 amorphous silicon flat panel digital X-ray imager, in reflection mode with a molybdenum target. An X-ray tube voltage of 40 kV, and a tube current of 285 μA were used, with an exposure of 500 ms, and a total of 1080 projections, with a voxel (3-D pixel) size of 52.73 μm. The tomograms were reconstructed from 2-D projections using a Nikon commercial software package (CTPro version 3.0, Nikon Metrology), a cone-beam reconstruction algorithm based on filtered back-projection. The commercial software VGStudio Max 2.1.5 was used to view the reconstructed data and produce 2-D grey scale slices.

The smaller sub-specimens were investigated at higher resolution using a lab-based Zeiss Xradia 520 (Carl Zeiss XRM, Pleasanton, CA, USA) X-ray Microscope, using a CCD detector system with scintillator-coupled visible light optics, and tungsten transmission target. For Specimen 2, sub-specimens 1-6, an X-ray tube voltage of 50 kV, and a tube current of 80 μA were used, with an exposure of 2000 ms, and a total of 3060 projections. An objective lens giving an optical magnification of 4 was selected with binning set to 2, producing an isotropic voxel (3-D pixel) sizes in the range 2.2906 μm to 2.2945 μm . The tomograms were reconstructed from 2-D projections using a Zeiss commercial software package (XMReconstructor, Carl Zeiss), a cone-beam reconstruction algorithm based on filtered back-projection. XMReconstructor was also used to produce 2-D grey scale slices for subsequent analysis. One sub-specimen from Specimen 1 was imaged along a 6.4mm length at high resolution, using an overlap-scan and stitching procedure including seven individual scans, with 15% overlap between each scan. The scan parameters were the same as the above Versa scans, but with a different source-sample-detector distance, resulting in a voxel size of 1.0487 μm.